Journal of Alloys and Compounds 650 (2015) 887–895

Contents lists available at ScienceDirect

Journal of Alloys and Compounds

journal homepage: http://www.elsevier.com/locate/jalcom

Effects of processing parameters on the morphology, structure, and magnetic properties of $Cu_{1-x}Fe_xCr_2Se_4$ nanoparticles synthesized with chemical methods

R.D. Ivantsov [a], I.S. Edelman [a, *], S.M. Zharkov [a, b], D.A. Velikanov [a, b], D.A. Petrov [a], S.G. Ovchinnikov [a, b], Chun-Rong Lin [c], Oksana Li [b, c], Yaw-Teng Tseng [c]

[a] Kirensky Institute of Physics, Russian Academy of Sciences, Krasnoyarsk, 660036, Russia
[b] Siberian Federal University, Krasnoyarsk, 660041, Russia
[c] National Pingtung University, Pingtung City, Pingtung County, 90003, Taiwan

ARTICLE INFO

Article history:
Received 15 June 2015
Received in revised form
31 July 2015
Accepted 2 August 2015
Available online 7 August 2015

Keywords:
Copper selenide
Magnetic nanoparticles
Visible magnetic circular dichroism

ABSTRACT

$Cu_{1-x}Fe_xCr_2Se_4$ nanoparticles with x = 0, 0.2, and 0.4 were synthesized via thermal decomposition of metal nitrate or chloride salts and selenium powder using different precursor compositions and processing details. Single crystalline nano-belts or nano-rods coexist in the synthesized powder samples with hexagon-shaped plates in dependence on the precursor composition. The belts gathered into conglomerates forming "hierarchical" particles. Visible magnetic circular dichroism (MCD) of $Cu_{1-x}Fe_xCr_2Se_4$ nanoparticles embedded into a transparent matrix was investigated for the first time. The similarity of the MCD spectra of all samples showed the similarity of the nanoparticles electronic structure independent of their morphology. Basing on the MCD spectral maxima characteristics, electron transitions from the ground to the excited states were identified with the help of the conventional band theory and the multi-electron approach.

1. Introduction

Chromium chalcogenide spinel $CuCr_2Se_4$ is a unique compound: high temperature ferromagnetism in combination with metal conductivity [1] provides a wide field of its applications. $CuCr_2Se_4$ characterized by the Curie temperature, T_c, near 430 K [2–5] and magnetic moment M_s of 5.07 μB/mol at 0 K [6], displays a large magneto-optical Kerr effect (KE) in the near infrared spectral region [7–9] and has highly spin-polarized characteristics [8,10]. So, it can be considered as a perspective material for spintronics. Several authors have undertaken attempts to modify $CuCr_2Se_4$ properties using the ion substitution methods. Thus, Cu^+ ion substitution by Li^+ ions in the polycrystalline $Cu_{1-x}Li_xCr_2Se_4$ (x = 0–0.7) samples resulted in the changes of the substance ground state from a ferromagnetic metal to a ferromagnetic insulator [11] and to a decrease of M_s. Se^+ ions substitution by Br^+ ions in $CuCr_2Se_{3.7}Br_{0.3}$ led to the shift of the KE maximum energy near 1 eV to the higher energy region. Interesting results were obtained when substituting Cu by other transition metals: Co [12,13], Ni [14], and Fe [15]. In the last case, the extreme members of the series $Cu_{1-x}Fe_xCr_2Se_4$ possess different structure and physical properties. In particular, $CuCr_2Se_4$ has a normal spinel structure [16] and is characterized by the ferromagnetic order below 433 K, while $FeCr_2Se_4$ has the monoclinic structure of the NiAs type [17] and possesses antiferromagnetic order below 218 K [18,19]. The authors of Ref. [15] showed that $Cu_{1-x}Fe_xCr_2Se_4$ bulk compounds crystallize with a spinel structure for $0 \le x \le 0.6$ and with a monoclinic structure for $0.9 \le x \le 1$. For $0.6 < x < 0.9$, the two phases coexist. They showed also that the charge states of the iron ions were ferric (3+) and ferrous (2+) in the spinel and monoclinic structures, respectively, and that the ferromagnetic super-exchange interactions dominated in the spinel phase, while the antiferromagnetic super-exchange interactions dominated in the monoclinic phase. Since that, only a few papers appeared in literature devoted to the investigation of $Cu_{1-x}Fe_xCr_2Se_4$ compounds. One of them was devoted to the electronic band structure calculation of $Cu_{0.5}Fe_{0.5}Cr_2Se_4$ using the full-potential augmented plane wave (FLAPW) method both in the generalized gradient approximation (GGA) and in the GGA + U (GGA incorporating the on-site Coulomb interaction) [20].

* Corresponding author.
E-mail address: ise@iph.krasn.ru (I.S. Edelman).

http://dx.doi.org/10.1016/j.jallcom.2015.08.017
0925-8388/

Several of methods are known to modify the substance properties including the production of materials in the nanostructured form of various morphologies. In the case of $CuCr_2Se_4$, a number of works are available in literature devoted to the nanoparticle synthesis by solution-based solve-thermal [21–25] and microwave [26] methods. Transition from the bulk to the nano-sized samples in the case of mixed compounds, for example $M1_{1-x}M2_xCr_2Se_4$ (M1 and M2 are the transition metals), could provide interesting effects such as the dependence of the phase transformation concentration on the nanoparticles size and morphology; strong dependence of the nanoparticle properties on the methods of their synthesis, and so on.

The present paper is devoted to the synthesis of $Cu_{1-x}Fe_xCr_2Se_4$ nanoparticles with $x = 0$, 0.2, and 0.4 using different precursor compositions and processing details. The nanoparticle morphology and structure as well as their magnetic properties are studied in connection with the processing peculiarities. Besides, the nanocomposite samples based on the particles embedded into a transparent matrix are fabricated to study the magneto-optical properties of $Cu_{1-x}Fe_xCr_2Se_4$ nanoparticles in the transmitted light. Magnetic circular dichroism (MCD) spectroscopy was chosen for this purpose since this technique makes the information easier for interpretation as compared to the methods based on the Faraday Effect (FE) and KE; it possesses high sensitivity and resolution power and can serve as a proper tool for the identification of electron transitions from the ground to the excited bands or levels in a matter.

2. Experimental

$CuCr_2Se_4$ nanoparticles were synthesized via the thermal decomposition of metal nitrates (samples 1 and 2) or chloride (samples 3–5) salts and selenium powder in a high-temperature organic solvent. In a typical process, we used 150.9 mg of copper nitrate, $Cu(NO_3)_2\cdot 3H_2O$, and 500 mg of chromium nitrate, $Cr(NO_3)_3\cdot 9H_2O$, together with 246.7 mg of Se powder to synthesize samples 1 and 2. The mixtures together with 20 ml of oleylamine (OLA), and 5 ml of oleic acid (OA) were put into a three-neck flask equipped with an inlet of argon gas, condenser, magnetic stirrer, thermocouple, and heating mantle. After the argon gas had been filled into the system during 10 min, the mixture was heated to 120 °C and maintained at this temperature for 0.5 h. Then the temperature rose to 200 °C and the mixture was aged for 0.5 h. Finally, the temperature of the reaction mixture rose to up to 340 °C and the mixture was aged for 3 h. After the mixture had been cooled down to room temperature, the obtained nanoparticles were separated from the suspension with a magnetic field. To remove the excess of the organic solvent and by-products completely, the products were washed several times with hexane by the magnetic decantation. The precursor components are listed in Table 1.

To synthesize samples 3–5 we used the same equipment and the thermal decomposition of the mixture of the metal-oleylamine (Cu–Fe–Cr–OLA) and selenium-oleylamine (Se-OLA) complexes. All the reactions were performed in a fume hood, under argon atmosphere conditions. The Cu–Fe–Cr–OLA complexes were prepared by dissolving an appropriate amount of CuCl, $FeCl_2\cdot 4H_2O$ and $CrCl_3\cdot 6H_2O$ in 10 mL of oleylamine (OLA) at 150 °C for 10 min, and then the mixture was cooled down to room temperature. The Se-OLA complexes were obtained by dissolving Se powder in 16.6 mL of OLA at 330 °C for 1 h. After the synthesized Se-OLA complexes had been cooled down to room temperature, the Cu–Fe–Cr–OLA complexes were poured into Se-OLA complexes. The resulting mixture was heated up to 200 °C and maintained at this temperature for 2 h. Subsequently, the reaction mixture was heated up to 350 °C, and then the temperature of the reaction mixture was decreased to 330 °C and aged for 1 h. After the mixture had been cooled down to room temperature, a mixture of hexane and ethanol was added to the solution, and the products could be separated via centrifugation. To remove the excess of the organic solvent and by-products completely, the products were washed several times with the mixture of hexane and ethanol. The details of the composition of the raw materials for preparing $Cu_{1-x}Fe_xCr_2Se_4$ nanoparticles are summarized in Table 2.

The morphology and structure of nanoparticles were determined with the high-resolution transmission electron microscope (HRTEM) JEOL JEM-2100 (LaB_6) with the accelerating voltage 200 kV equipped with the energy dispersive X-ray spectrometer Oxford Inca x-sight and a complex for sample preparation including Gatan Precision Ion Polishing System (PIPS). Selected-area electron diffraction (SAED) was used to determine the structure of the nanoparticles.

Magnetization temperature dependences were studied with the SQUID magnetometer at temperatures 4.2–450 K in the magnetic field 0.02 T both for the nanoparticles powder and for the composite samples purposely prepared for magnetooptical measurements (see below). For several samples magnetic measurements were carried out also with the vibrating sample magnetometer (VSM) at temperatures 77–300 K in magnetic field up to 0.6 T. The magnetization was measured in the course of sample heating after cooling them in one of the two different regimes: in the presence of an external magnetic field (FC) and without a magnetic field (ZFC). The magnetization curves were recorded also with the vibrating sample magnetometer at several temperatures.

MCD was measured in the normal geometry: the magnetic vector and the light beam were directed normal to the sample plane. The modulation of the light wave polarization state from the right-hand to the left-hand circular polarization relatively to the magnetic field direction was used for the MCD measurements. The modulator was made of a fused silica prism with a glued piezoelectric ceramic element. In the absence of an acoustic excitation, the prism is optically isotropic. When the ac voltage of frequency ω corresponding to the eigen-frequency of the system is supplied to the piezoelectric ceramics, an elastic stationary wave will be excited in the quartz prism. Linearly polarized light with the polarization plane turned to an angle of 45° relatively the horizontal prism axis falls on the prism. At the exit of the prism, the light wave will acquire circular polarization when a stationary acoustic wave is excited in it. This polarization changes from the right-to the left-hand circle during one period of acoustic vibration of the prism. The AC voltage on the modulator was set taking into account the light wave length. In the case of a sample possessing MCD, its absorption coefficients are different for the right- and left-hand

Table 1
Precursor compositions of $CuCr_2Se_4$ powder samples No's 1 and 2.

Sample no	Precursor components
1	$Cu(NO_3)_2\cdot 3H_2O + Cr(NO_3)_3\cdot 9H_2O$ + Se powders
2	$Cu(NO_3)_3\cdot 6H_2O + Cr(NO_3)_3\cdot 9H_2O$ + Se powders

Table 2
Precursor compositions (g) of $Cu_{1-x}Fe_xCr_2Se_4$ powder samples No's 3–5.

Sample no	X	CuCl	$FeCl_2\cdot 4H_2O$	$CrCl_3\cdot 6H_2O$	Se
3	0.0	0.0662	0.0000	0.3560	0.5274
4	0.2	0.0530	0.0266	0.3560	0.5274
5	0.4	0.0396	0.0531	0.3560	0.5274

circular polarized light waves with respect to the magnetic moment direction of a sample. As a result, the light flux having passed through the sample and reaching a photomultiplier has a modulated intensity. The MCD value was measured as the difference between the photomultiplier voltages for two opposite directions of an applied magnetic field in the spectral range 1.2–3.6 eV in a magnetic field up to 1.2 T in the temperature range 95–300 K. The measurement accuracy was about 10^{-4}, and the spectral resolution was 20–50 cm^{-1} depending on the wavelength. Conventional phase-sensitive detection technique of the electric signal was used to get rid of electrical and mechanical noises.

To realize magneto-optical measurements, transparent composite samples containing the nanoparticles were prepared: the nanoparticles powder was mixed with dielectric transparent silicon-based glue ("Rayher" art. nr. 3338100 80 ml) in the weight proportion 0.5/100 and measures were undertaken to obtain the homogeneous particle distribution in the matrix such as the mixture treatment in the ultrasonic bath. The low magnetic powder concentration allows excluding the interaction between the nanoparticles. The mixture was placed between two thin glass plates spaced by wires of 0.15 mm in diameter and solidified.

3. Results and discussion

3.1. Nanoparticles morphology and structure

Two types of nanoparticles were observed in all the powdered samples: thin plates of approximately hexagonal shape and elongated particles, like belts or rods. In the case when metal nitrates were used as precursors (samples No's 1 and 2), belts of 20–30 nm in length and ~5 nm in width transparent for electron flow were observed (Figs. 1b and 2b). They gathered in more or less large conglomerates similar to hierarchical nanoparticles consisting of many sub-nanometer components. In spite of small lateral dimensions of the belts, they demonstrated distinct atomic planes (Fig. 1b) with the same spacing, 0.60 nm, characteristic of the $CuCr_2Se_4$ (111) plane as in the relatively large plate-like particles (Fig. 1c). In the case when metal chlorides were used as precursors (samples No 3), rods of 30–60 nm in length and ~5 × 5 nm^2 in cross-section were observed (Fig. 3a, b). The replacement of Cu for Fe at relatively low concentrations (sample No 4) leads to a marked increase of rods fraction with respect to the hexagonal nanoparticles (Fig. 3c). One can note that the rods seemed to be arranged parallel and very close to each other. The thin flat nanoparticles in samples No's 3 and 4 have an almost ideal hexagonal shape and approximately the same dimensions of about 50 nm (Fig. 3a). According to SAED data (an example is shown in Fig. 1d), all the nanoparticles described above have the $CuCr_2Se_4$ crystal structure, space group Fd3m, a = 10.337(6) Å (PDF Card #04-007-5505). A higher Fe concentration leads to the appearance of a different shape and dimension of the nanoparticles (Fig. 3e and f) and to the appearance of additional reflexes in the SAED picture that can be associated, more probably, with the phase $Cu_{0.5}Fe_{0.5}Cr_2Se_4$ (Fd3m, a = 9.91 Å), PDF #04-002-6588. Nevertheless, most of the nanoparticles preserve the same structure as observed in samples No's 1–4.

Finalizing this part, we can assert that the precursor composition strongly affects the nanoparticle morphology and arrangement. For the same basic precursor composition, the nanoparticle morphology and arrangements depend on the degree of the Cu

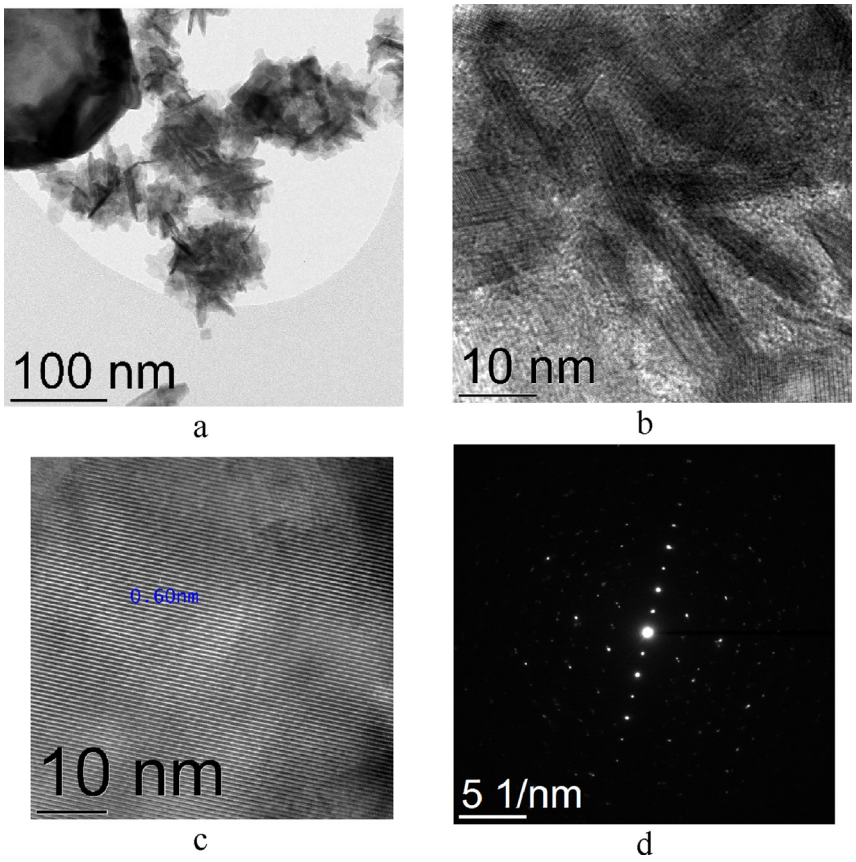

Fig. 1. TEM (a) and HRTEM images of the belts and plate-like particles (b and c, correspondingly) and SAED patterns (d) of powdered $CuCr_2Se_4$ sample No 1.

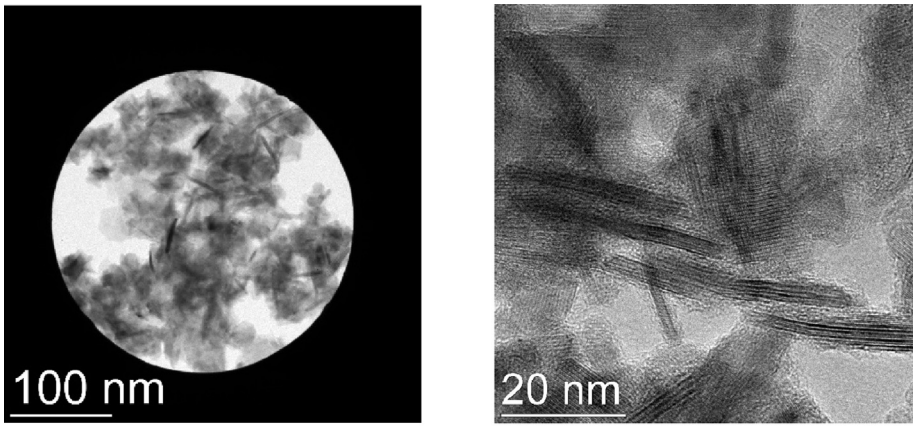

Fig. 2. TEM (a) and HRTEM (b) images of powdered $CuCr_2Se_4$ samples No 2.

substitution by Fe. In all the cases, the nanoparticles are crystalline.

It should be noted that in the case of the nitrate precursors (samples No's 1 and 2), the nanoparticles arising could be referred to the so-called hierarchical nanoparticles. This new type of nanoparticles consisting of many sub-nanometer components of different morphology has attracted considerable attention during the two last decades [27–32]. Materials constructed of hierarchical nanoparticles exhibit distinctive properties different from those of uniform nanoparticles and bulk materials. It makes them promising for potential applications in a variety of fields such as lithium batteries, catalysts, magnetic materials, drug delivery, etc. Among them, transition metal chalcogenides (double selenides and sulfides) with hierarchical three-dimensional nanostructures are considered as the perspective electrode materials for rechargeable lithium ion batteries [27,31]. Hierarchical nanostructures of tertiary chalcogenides could be of interest for this field also because of their poly-functionality. At any rate, the insertion of Li into the $CuCr_2Se_4$ spinel structure was considered in Ref. [33] Hierarchical nanoparticle morphology could intensify this process.

3.2. Magnetic properties of the nanoparticles

The ZFC and FC magnetization temperature dependence for five powdered samples measured in the magnetic field H = 0.02 T are shown in Fig. 4. The Curie temperatures (T_c) of all the samples estimated from the maximum position of the M (T) derivative with respect to temperature are collected in Table 3. For samples No's 1 and 2, T_c is close to the literature data for the bulk $CuCr_2Se_4$ [2–4].

For sample No 3, T_c is lower which can be associated with the nanoparticles morphology or, most likely, with uncontrolled inclusions changing distances between the interacting magnetic ions. The T_c value decreases further with the increase of the Fe concentration (samples No's 4 and 5). The decrease, particularly strong for sample No 5, may be due to the appearance of the local antiferromagnetic super exchange interactions, that is, to the appearance of an intermediate state between ferromagnetic $CuCr_2Se_4$ and antiferromagnetic $FeCr_2Se_4$ phases. In the case of the bulk compounds, the intermediate states appear for $0.6 < x < 0.9$ [15]. In the case of the nanoparticles, the phase boundaries may shift to the lower Fe concentrations.

The shape of the magnetization temperature dependence resembles superparamagnetic relaxation when considering that the ZFC and FC magnetization bifurcate, and the ZFC curve demonstrates a broad peak. The broad peak is observed also in the FC curves 1–4. This peak is seen even for the significantly higher measurements field (Fig. 5a). Fig. 5b demonstrates the identity of the temperature magnetization behavior for both types of the samples: the nanoparticles powder and nanoparticles containing composite that was used for the magnetooptical experiments. The irreversibility temperatures corresponding to the bifurcation points are higher than the room temperature. Thus, at least, some portions of the nanoparticles are in the "frozen" state already at room temperature. The peaks in the FC curves may evidence that some nanoparticles possess anisotropy strong enough to stay oriented randomly after cooling in the magnetic field (here 0.02 T).

Typical hysteresis loops of the nanoparticle powder samples recorded with VSM and of a nanocomposite sample recorded with the use of MCD are shown in Fig. 6. Analogously to the magnetization temperature dependences, the hysteresis loops shape is the same for both types of the samples. The room temperature loops allow considering most of the nanoparticles to be in the super paramagnetic state, but some nanoparticles are frozen, coercive field equals to 0.02 T. The saturation magnetization, saturation field, and coercivity increase strongly with the temperature decrease.

Summarizing the magnetization behavior of the nanoparticles under an action of the temperature and magnetic field, one can ascribe the peculiarities of this behavior to the complex particle morphology, in particular, to the prolong shape of some portion of the nanoparticles.

3.3. Magnetic circular dichroism

Typical MCD spectra recorded at H = 0.3 T directed normal to the sample plane and two temperatures 90 and 295 K for the composite samples are shown in Fig. 7. Several extremes of the opposite sign are observed in the spectra. The extreme positions in the energy interval 1.2–3.5 eV are almost the same for all the samples, but their intensity distribution changes from sample to sample. The MCD spectra of sample No 1 resemble the Kerr rotation (KR) spectrum of the bulk $CuCr_2Se_4$ single crystals presented in Refs. [7,9]. Especially close these MCD spectra are to the imaginary part of the off-diagonal conductivity shown in Fig. 3 in Ref. [9]. Generally, the coincidence of the KR and MCD spectra seems to be quite natural because both effects: MCD (θ_F) and KR (θ_K) are described by the similar equations [34]:

$$\theta_F = \frac{4\pi}{\lambda}\left\{\frac{n}{k^2+n^2}\varepsilon''_{xy} - \frac{k}{k^2+n^2}\varepsilon'_{xy}\right\} \quad (1)$$

and

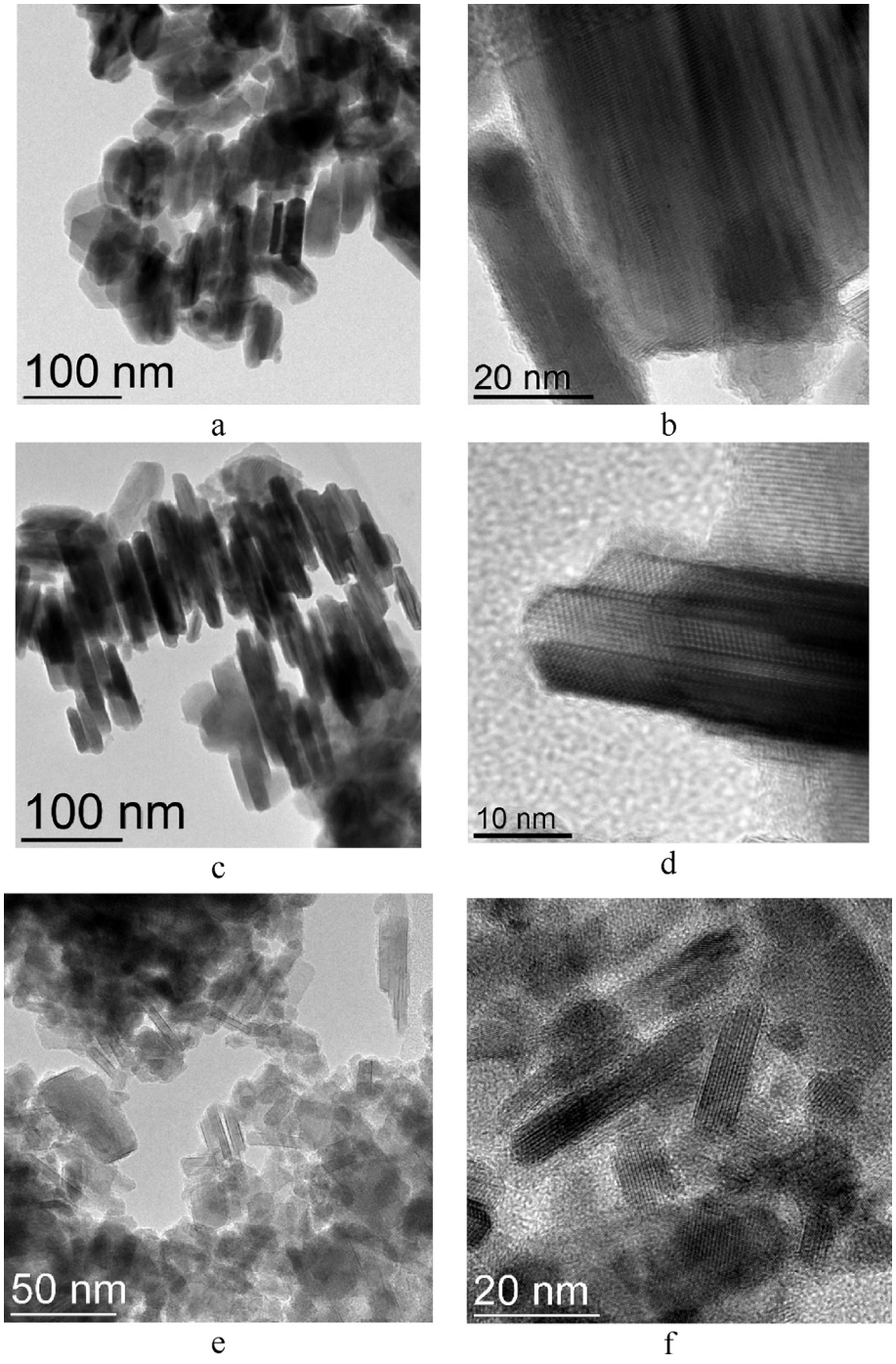

Fig. 3. TEM (a, c, e) and HRTEM (b, d, f) images of powdered samples No 3 (a, b), No 4 (c, d), and No 5 (e, f).

$$\theta_K = \frac{B}{B^2 - A^2}\varepsilon''_{xy} - \frac{A}{B^2 - A^2}\varepsilon'_{xy}, \quad (2)$$

where ε'_{xy} and ε''_{xy} are the real and imaginary parts of the off-diagonal component of the dielectric tensor ε, n and k are the refractive index and absorption coefficient, respectively, λ is the light wave length, $A = (n^3\text{-}3nk^2\text{-}n)$ and $B = (3n^2\text{-}k^3)$. However, as compared to the Kerr spectra [9], the MCD spectra in the visible region seem to be more distinct and containing more features. In order to extract meaningful information from the MCD data and make adequate comparison between the samples, we carried out the MCD spectra decomposition to several Gaussian components. Different approaches are possible to the MCD spectra decomposition. We supposed all the visible extremes, both positive and negative, to be of the paramagnetic line shape based on different behavior of their amplitudes when coming from sample to sample and at the temperature change. To obtain the best fitting to the experimental spectra, we should introduce a peak near E = 1.0 eV which is beyond our available spectral region. The validity of including this peak into consideration is proved by its complete coincidence with the strongest KR peak near the energy 1.2 eV observed by all the authors dealing with KR and ascribed to the

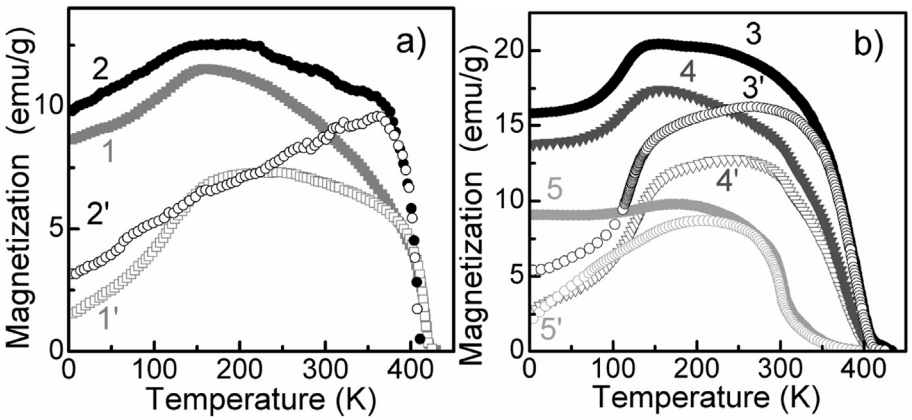

Fig. 4. The FC (curves 1–5) and ZFC (curves 1′–5′) magnetization temperature dependences for samples No's 1–2 (a) and 3–5 (b). Curve numbers correspond to the sample numbers (Tables 1 and 2). H = 0.02 T.

Table 3
Curie temperatures, T_c, of the powdered samples.

Sample no	1	2	3	4	5
T_c, K	416	410	385	374	300

plasmon excitations [7–9]. We denote this peak as E_0. For the best fitting, we include also the high-energy peak situated out-of the limits of the investigated spectral interval. Examples of the fitting are shown in Fig. 8. The parameters of the decomposition components best fitted to experimental data are collected in Tables 4–6.

Energy positions of the definite peaks (Table 4) are close with each other for all the samples. The peak energy shift at the temperature decrease from 295 to 90 K is very small. Some peaks demonstrate the shift to higher energies (E_1, E_2, and E_4) for all the samples, while other peaks (E_0, E_3, E_5) shifts are of different sign for different samples. The peak intensity changes more significantly while coming from sample to sample, as it is seen from Table 5, where the relative values of the peak intensity in each sample are collected. The relative peak intensities were determined in such a way: for each sample, the maximal peak intensity was taken as a unit; the intensities of all other peaks were determined relatively to this one. The peak E_0 was excluded from this consideration as it was not observed experimentally and, on the other hand, we wanted to show clearly the intensity distribution between E_1-E_5 peaks.

The close coincidence of the MCD peak energies for all the samples testifies the identity of their electron energy structure. At the same time, different intensities of the same peaks in different samples can be associated with different probabilities of the electron transitions between the energy bands or levels. Comparing the peak energy positions with the density of the states (DOS) calculated for $CuCr_2Se_4$ in several works [1,8,9], we can ascribe the strong negative peak E_3 to the transition Se4p↓ → Cr3d↓ (Fig. 4 in Ref. [8]) and the positive peak E_5 to the transition Se4p↑ → Cr3d↑ (Fig. 4 in Ref. [8]). The weaker peaks E_2 and E_4 can be assigned to the on-site d–d transitions of chromium ions $^4A_2(t_2^3) \rightarrow {}^4T_2(t_2^2e)$ and $^4A_2(t_2^3) \rightarrow {}^4T_1(t_2^2e)$, correspondingly. Note that the maximum near 1.9 eV observed in the KR spectrum in Ref. [9] was assigned to the Cr d–d transition too. The question on the origin of the peak E_1, observed so distinct only with the MCD technique, stays opened within the band theory. The band structure of chromium spinel was studied earlier within the multi-electron approach with account for strong electron correlations of 3d (Cr) electrons [35,36]. According to this approach, the energies of d–d transitions of chromium ions are very close to the measured E_2 and E_4 peaks. The peak E_1 may result from the $t_{2g}(Cr) \rightarrow p(Se)$ excitations from the $^3T_1(t_{2g}^2)$ filled state of Cr^{4+} to the empty states of p (Se) electrons at the top of the valence band $CuCr_2Se_4$ [35]. This peak is the most sample dependent. Different sample processing may result in particular impurity states above the top of the valence band. That is why, the energy E_1 and the peak intensity varies stronger from sample to sample as compared to other peaks. Thus, the characteristic energies of the

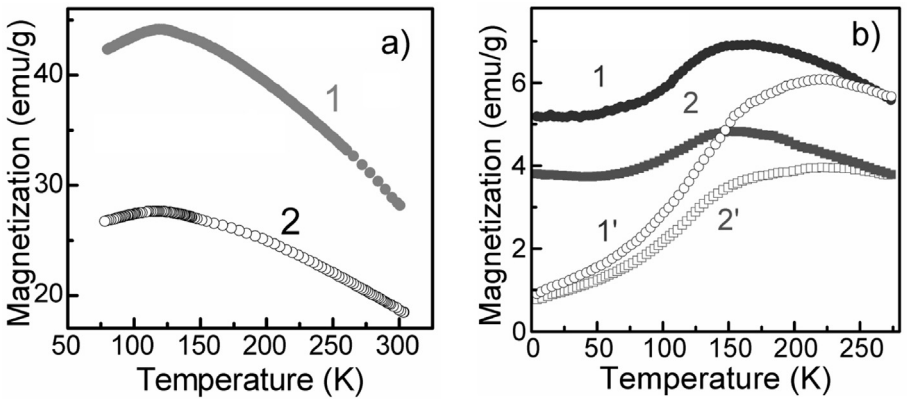

Fig. 5. a – FC magnetization temperature dependences of samples No's 1 and 3 recorded with VSM at H = 0.35 T b – Comparison of the FC and ZEC magnetization temperature dependences for powdered (1 and 1′ curves) and nano-composite (2 and 2′ curves) samples No 1.

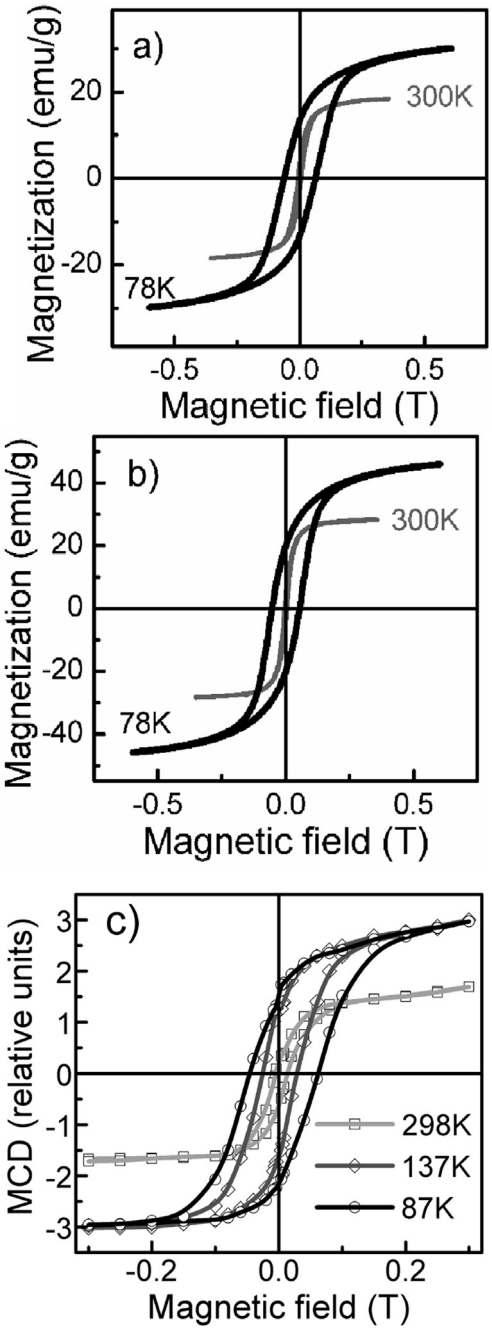

Fig. 6. Magnetization hysteresis loops of samples No's 1 and 3 (a and b, correspondingly) recorded with VSM and (c) of a nano-composite sample with nanoparticles No 1 obtained with MCD measurements at 1.28 eV.

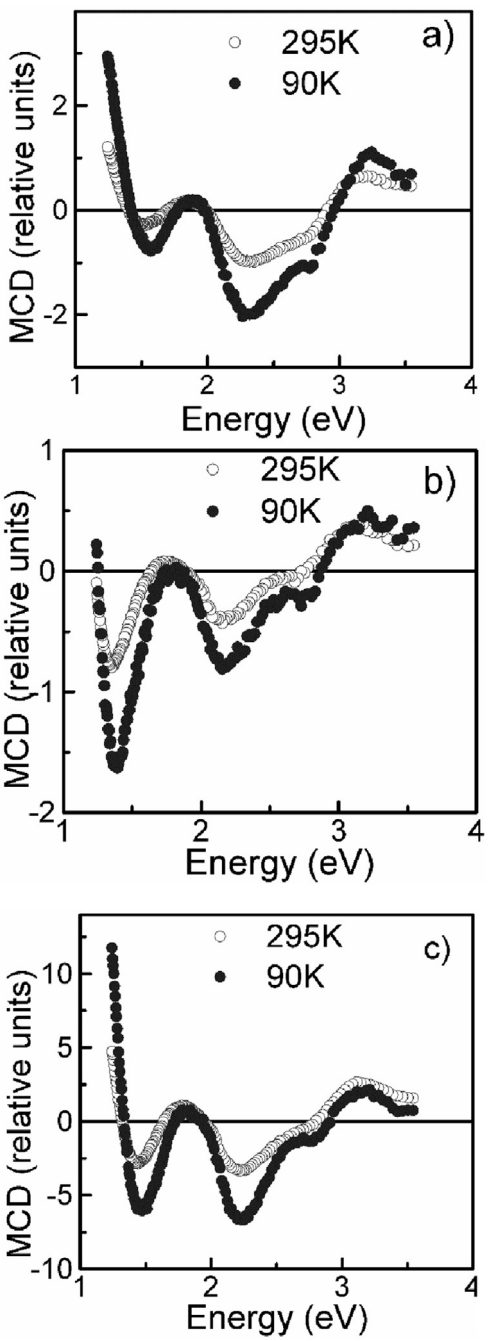

Fig. 7. MCD spectra of nano-composite samples containing nanoparticles No's 1 (a), 3 (b), and 2 (c) recorded at 90 and 295 K, H = 0.35 T.

peaks E_2-E_5 forming the MCD signal correlate satisfactory with the electron transition energies in $CuCr_2Se_4$ obtained from both the conventional band theory and the multi-electron approach. The last one allows identifying also the peak E_1.

4. Conclusion

We have studied the morphology and magnetic properties, including magneto-optics, of $Cu_{1-x}Fe_xCr_2Se_4$ nanoparticles synthesized via thermal decomposition of metal nitrate or chloride salts and selenium powder with different ratios of the raw material components in the high-temperature organic solvent. Correlations between technological conditions and nanoparticles morphology, on one hand, and between the morphology and magnetic properties of nanoparticles, on the other hand, are obtained. According to the high-resolution transmission electron microscopy data, nanoparticles of two types coexist for all raw material compositions: thin hexagon plates and thin belts (for nitrate salts) or rods (for chloride salts). Moreover, all types of the nanoparticles are single crystalline ones with the $CuCr_2Se_4$ structure, besides the particles with $x = 0.4$ demonstrated a more complicated structure. For some compositions, the belts gather into large conglomerates forming hierarchical particles. The magnetization temperature dependences of the nanoparticles demonstrate different shapes for FC

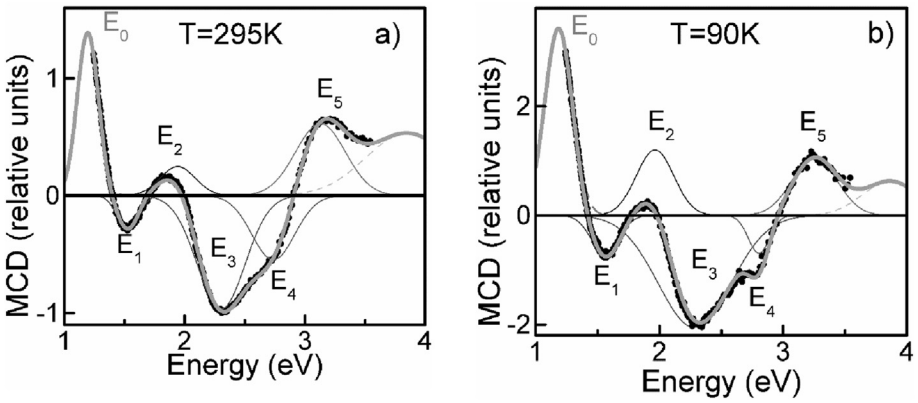

Fig. 8. Decomposition of the sample No 1 MCD spectrum for the temperatures 295 (a) and 90 K (b).

Table 4
Energies of the MCD peaks in the nano-composite samples.

Peak no	Sample no 1		Sample no 2		Sample no 3		Sample no 4		Sample no 5	
	E, eV		E, eV		E, eV		E, eV		E, eV	
	295 K	90 K	295 K	90 K	295 K	90 K	295 K	90 K	295 K	90 K
E_0	1.19	1.18	1.17	1.14	1.20	1.17	1.20	1.19	1.20	1.20
E_1	1.53	1.56	1.35	1.38	1.44	1.48	1.48	1.51	1.47	1.49
E_2	1.94	1.96	1.81	1.88	1.83	1.91	1.84	1.90	1.80	1.91
E_3	2.30	2.28	2.18	2.19	2.23	2.23	2.25	2.24	2.33	2.32
E_4	2.74	2.80	2.71	2.80	2.68	2.74	2.65	2.81	2.77	2.85
E_5	3.13	3.25	3.10	3.11	3.12	3.16	3.16	3.21	3.27	3.23

Table 5
Relative MCD peak amplitudes of the nano-composite samples at 295 K.

Sample no	E_1	E_2	E_3	E_4	E_5
	Relative values of the peak amplitudes				
1	0.296	0.258	1.00	0.565	0.636
2	1.00	0.140	0.517	0.782	0.460
3	1.00	0.330	1.00	0.246	0.660
4	1.00	0.424	1.00	0.600	1.00
5	1.00	0.098	0.831	0.758	0.253

Table 6
The ratios of the peak's intensities at 90 K to that at 295 K.

Sample no	E_o	E_1	E_2	E_3	E_4	E_5
	I_{90}/I_{295}					
1	3.13	3.156	5.03	4.15	0.61	1.5
2	3.85	2.389	1.67	2.12	0.66	1.8
3	4	2.61	1.33	1.5	1.08	0.87
4	2.88	2.92	2.50	3.61	0.60	1.75
5	3.96	4.3	4.6	2.59	2.89	10

and ZFC modes characteristic for heterogeneous systems such as super paramagnetic particles. However, contrary to usual situations, the magnetization maximum is observed not only in ZFC but also in the FC curve. The maxima positions and widths depend on the nanoparticle morphology. The Curie temperature for all the samples with $x = 0$ is about 400 K; it decreases with the x value increase. Magnetic circular dichroism (MCD) spectra demonstrate several extremes of different signs in the region 1.2–3.5 eV. The similarity of the MCD spectra for all the samples evidences the same nanoparticle electronic structure depending weakly on their morphology. Using the spectra decomposition into Gaussian components, we presented them as a sum of two positive and three negative peaks and determined all peaks characteristics. The characteristic energies of the peak gravity centers change insignificantly when coming from sample to sample contrary to their intensities, which can change at that in several times. Explanation of most of the peaks from the conventional band theory and the multi-electron approach are in the qualitative agreement. The lower energy peak (E_1), most sensitive to the sample, found its explanation in the frame of the multi-electron approach only.

Acknowledgements

The paper was partially supported by the Russian Foundation for Basic Research (grant #14-02-01211), by the President of Russia (grant #NSh-2886.2014.2), and by the Ministry of Education and Science of the Russian Federation (grant #2014/71/1763 in the framework of the state assignment for the Siberian Federal University for 2014–2016). We also thank the Ministry of Science and Technology of Taiwan and the Siberian Branch of RAS (MOST 102-2112-M-153 -002 -MY3) for financial support.

References

[1] J.S. Bettinger, R.V. Chopdekara, M. Liberati, J.R. Neulingere, M. Chshiev, Y. Takamura, L.M.B. Alldredgea, E. Arenholz, Y.U. Idzerda, A.M. Stacy, W.H. Butlerf, Y. Suzuki, J. Magn. Magn. Mater 318 (2007) 65.
[2] I. Nakatani, H. Nose, K. Masumoto, J. Phys. Chem. Sol. 39 (1978) 743.
[3] M.H. Robbins, W. Lehman, J.G. White, J. Phys. Chem. Sol. 28 (1967) 897.
[4] H. Mamiya, I. Nakatani, Nanostructured Mater 12 (1999) 859.
[5] M.D. Anderson, J.O. Thompson, D.C. Johnson, Chem. Mater 25 (2013) 3996.
[6] F.K. Lotgering, R.P. Van Stapele, J. Appl. Phys. 39 (1968) 417.
[7] H. Brandle, J. Schoenes, P. Wachter, F. Hulliger, W. Reim, Appl. Phys. Lett. 56 (1990) 2602.
[8] V.N. Antonov, V.P. Antropov, B.N. Harmon, A.N. Yaresko, A. Ya. Perlov, Phys. Rev. B 59 (1999) 14552.
[9] S. Bordács, I. Krzsmarki, K. Ohgushi, Y. Tokura, New J. Phys. 12 (2010) 053039.
[10] F. Ogata, T. Hamajima, T. Kambara, K.I. Gondaira, J. Phys. C. Sol. St. Phys. 15

(1982) 3483.
[11] R. Li, Z. Qua, L. Zhang, L. Ling, W. Tong, Y. Zhang, Sol. St. Commun. 150 (2010) 2289.
[12] S.G. Smirnov, A.W. Rozancew, J.A. Kesler, I.W. Gordiejew, J.D. Trietiakow, Neorg. Mater 19 (1983) 886 (in Russian).
[13] E. Maciazek, A. Molak, T. Goryczka, J. Alloys Comps 441 (2007) 222.
[14] I. Jendrzejewska, P. Zajdel, T. Gron, H. Duda, T. Mydlarz, J. Alloys Comps 593 (2014) 158.
[15] H.N. Ok, Yu Chung, Ju. G. Kim, Phys. Rev. B 20 (1979) 4550.
[16] R.W.Q. Wyckoff, Crystal Structures, vol. III, Wiley-Interscience, New York, 1964, p. 78.
[17] M. Chevreton, Acta Crystallogr. *A* 16 (1963) 22.
[18] L. Morris, P. Russo, A. Wold, J. Phys. Chem. Sol. 31 (1970) 635.
[19] K. Kojima, M. Matsui, K. Sato, K. Adachi, J. Phys. Soc. Jpn. 29 (1970) 1643.
[20] B.I. Min, S.S. Baik, H.C. Choi, S.K. Kwon, J.-S. Kang, New J. Phys. 10 (2008) 055014.
[21] M.L. Rao, M. Shamsuzzoha, A. Gupta, J. Cryst. Growth 306 (2007) 321.
[22] G.M. Tsoi, L.E. Wenger, Y.-H.A. Wang, A. Gupta, J. Magn. Magn. Mater 322 (2010) 142.
[23] K. Ramesha, R. Seshadri, Sol. St. Sci. 6 (2004) 841.
[24] Y. Aktas, O. Akman, M. Ozdem, Balk. Phys. Lett. 16 (2009) 161053.
[25] C.-R. Lin, C.-L. Yeh, S.-Z. Lu, I.S. Lyubutin, S.-C. Wang, I.P. Suzdalev, Nanotechnology 21 (2010) 235603, 6pp.
[26] D. Kim, A.N. Rusnak, S. Parameswaran, C.R. Patra, V.B. Trofimov, R. Harpness, A. Gedanken, YuS. Tveryanovich, Glass. Phys. Chem. 32 (2006) 330.
[27] Y. Wang, Q. Zhu, L. Tao, X. Su, J. Mater. Chem. 21 (2011) 9248.
[28] B. Wang, H. Wu, L. Yu, R. Xu, T.T. Lim, X.W. Lou, Adv. Mater 24 (2012) 1111.
[29] J.Y. Lao, J.Y. Huang, D.Z. Wang, Z.F. Ren, J. Mater. Chem. 14 (2004) 770.
[30] X. Liu, Y. Lin, S. Zhou, S. Sheehan, D. Wang, Energies 3 (2010) 285.
[31] Z. Zhou, W. Zhang, W. Zhao, Z. Yang, C. Zeng, J. Electron. Mater 43 (2014) 359.
[32] C. Zhang, Z. Lin, Zh. Yang, D. Xiao, P. Hu, H. Xu, Yu. Duan, Sh. Pang, L. Gu, G. Cui, Chem. Mater 27 (2015) 2189.
[33] W. Bensch, J. Ophey, H. Hain, H. Gesswein, D. Chen, R. Monig, P.A. Gruber, S. Indris, Phys. Chem. Chem. Phys. 14 (2012) 7509.
[34] A.K. Zvezdin, V.A. Kotov, Modern Magnetooptics and Magnetooptical Materials, IOP Publishing, Bristol and Philadelphia, 1997.
[35] S.G. Ovchinnikov, Fiz. Tverd. Tela 21 (1979) 2994 (in Russian).
[36] S.G. Ovchinnikov, Phase Transitions 36 (1991) 15.